
A Comprehensive Study and Comparison of the Robustness of 3D Object Detectors Against Adversarial Attacks

Yifan Zhang, Junhui Hou, Yixuan Yuan

Received: 16 December 2022

Abstract Deep learning-based 3D object detectors have made significant progress in recent years and have been deployed in a wide range of applications. It is crucial to understand the robustness of detectors against adversarial attacks when employing detectors in security-critical applications. In this paper, we make the first attempt to conduct a thorough evaluation and analysis of the robustness of 3D detectors under adversarial attacks. Specifically, we first extend three kinds of adversarial attacks to the 3D object detection task to benchmark the robustness of state-of-the-art 3D object detectors against attacks on KITTI and Waymo datasets, subsequently followed by the analysis of the relationship between robustness and properties of detectors. Then, we explore the transferability of cross-model, cross-task, and cross-data attacks. We finally conduct comprehensive experiments of defense for 3D detectors, demonstrating that simple transformations like flipping are of little help in improving robustness when the strategy of transformation imposed on input point cloud data is exposed to attackers. Our findings will facilitate investigations in understanding and defending the adversarial attacks against 3D object detectors to advance this field.

Keywords 3D object detection · Point cloud · Adversarial attack · Robustness evaluation

1 Introduction

3D object detection, which aims to identify and localize the 3D bounding boxes of objects in specific classes, has been

Yifan Zhang, Junhui Hou
Department of Computer Science, City University of Hong Kong.
E-mail: yzhang3362-c@my.cityu.edu.hk; jh.hou@cityu.edu.hk;

Yixuan Yuan
Department of Electronic Engineering, The Chinese University of Hong Kong.
E-mail: yxyuan@ee.cuhk.edu.hk

one of the most popular research fields of computer vision. The advancement brought about by deep learning-based approaches broadens the applications of 3D object detection to diverse fields, such as autonomous driving, domestic robots, and virtual reality. While deep learning in 3D object detection has achieved revolutionary performance in recent years, the robustness of detectors has not been sufficiently investigated.

Existing studies show that deep neural networks are vulnerable to adversarial examples, which are intentionally generated to fool the network (Szegedy et al., 2013). The vulnerability may subsequently cause serious security problems and thus raise concerns on the deployment of neural networks in safety-critical applications. We should also avoid similar potential risks of security in the application of 3D object detection, considering that the deteriorated predictions under attack (see Figure 1) will inevitably affect the reliability and stability of the system adopting 3D detectors. Therefore, the safety issues imply that the robustness of detectors against adversarial examples could be as important as the absolute accuracy on clean inputs.

To address the security issues, numerous attack (Goodfellow et al., 2014; Madry et al., 2018) and defense (Dziugaite et al., 2016) methods have been proposed in the 2D image domain. Besides, much effort of researchers is devoted to exploring attack and defense on learning-based 3D point cloud models (Xiang et al., 2019; Liu and Hu, 2022). Unfortunately, these existing works mainly concentrate on the task of point cloud classification, while the robustness of widely-used LiDAR-based 3D object detection, a significantly more complex task than point cloud classification, has not been systematically studied. Several works (Tu et al., 2020; Abdelfattah et al., 2021) generate adversarial examples by placing adversarial objects on the rooftop of target vehicles and successfully mislead 3D detectors, which can be attributed to the lack of relevant training data and mitigated by data

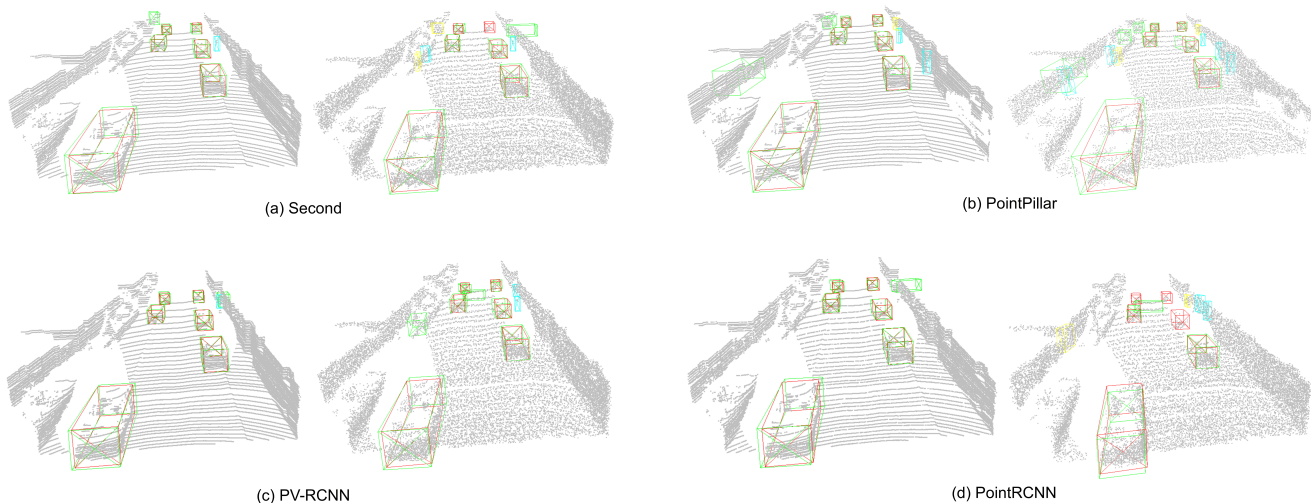


Fig. 1: Visual comparison of results predicted by various 3D detectors on clean input and under PGD-based point perturbation attack ($\epsilon=10\text{cm}$). For each comparison, the detection results on adversarial examples are shown on the right. The predicted bounding boxes of **car**, **pedestrian**, and **cyclist** are visualized in green, cyan, and yellow, respectively. The **ground-truth** bounding boxes are visualized in red. Best viewed in color and zoom in for more details. We can clearly observe the various detectors output deteriorated predictions, i.e., more false positive boxes and ground-truth boxes not detected, under adversarial attacks.

augmentation. By contrast, we extend three commonly used and less restrictive adversarial attacks to LiDAR-based 3D object detection, including point perturbation, detachment, and attachment attack, which are plausible even without the presence of the malicious attacker considering the inevitable range error of LiDAR sensor and other factors.

In this paper, we comprehensively investigate the robustness of LiDAR-based 3D detectors against adversarial attacks. Specifically, we extend three types of adversarial attacks to LiDAR-based 3D object detection, including point perturbation, detachment, and attachment. We rigorously evaluate the robustness of eight state-of-the-art 3D detectors with various architectures and feature representations on two popular datasets, i.e., KITTI and Waymo (Sun et al., 2020b) datasets. Besides, considering there may be no direct access to the target detectors, we also study the potential vulnerability of detectors under black-box attacks. The results imply that the adversarial examples generated from vulnerable detectors like PointRCNN (Shi et al., 2019) are transferable to other detectors. The comprehensive evaluation results suggest which state-of-the-art models for 3D object detection should be preferred in safety-critical applications.

In summary, the main contributions of this paper are:

- we extend three kinds of adversarial attacks to LiDAR-based 3D object detection, including point perturbation, detachment, and attachment;
- we benchmark the robustness of detectors with different feature representations, architectures, and model sizes against the adversarial attacks on KITTI and Waymo datasets;

- our experimental observations reveal that the voxel-based detectors are generally more robust than point-based detectors and some widely accepted observations in other fields are not applicable to 3D object detection.
- we identify the inherent disadvantages of the point perturbation attack when applied to voxel-based detectors, which make the attack less effective. We discuss the influence of re-voxelization and voxel size on the robustness of voxel-based detectors;
- we provide an extensive evaluation of the effectiveness of the black-box attack, i.e., the transferability of adversarial attacks including cross-model, cross-task, and cross-domain transferred attacks;
- we provide a thorough evaluation of various defense strategies against adversarial attacks and conclude that the defense of simple transformation turns out to be of little help to improve the robustness assuming the defense strategy is publicly available knowledge for attackers.

To the best of our knowledge, this is the first comprehensive evaluation and rigorous analysis of robustness of the 3D object detectors. We believe this work will facilitate future efforts in improving the robustness and reliability of the 3D object detectors against adversarial attacks without compromising detection accuracy. The remainder of the paper is organized as follows. Section 2 reviews existing works on LiDAR-based detectors and adversarial attacks. In Section 3, we extend three adversarial attacks against 3D object detection, followed by nine defense strategies in Section 4. 5 presents the setting of experiments in detail. We experimen-

tally evaluate and analyze the robustness of state-of-the-art model against various adversarial attacks in Section 6, and the black-box attacks in Section 7. In Section 8, we validate the effectiveness of commonly used defense strategies in point cloud tasks. Finally, Section 9 concludes this paper.

2 Related Work

2.1 LiDAR-based 3D Object Detection

We can roughly classify 3D object detection into two groups. 1) Typically, voxel-based 3D detectors turn point clouds into grid-structure forms with fixed sizes. Early work VoxelNet (Zhou and Tuzel, 2018) first proposed to convert the point cloud to a regular volumetric representation by stacked voxel feature encoding. Because it is not efficient to extract features with conventional convolution network because of the sparsity of non-empty voxels, Yan et al. (2018) introduced a more efficient sparse convolution to accelerate training and inference. Lang et al. (2019a) deployed a novel encoder that learns features on pillars (vertical columns) of the point clouds, where only 2D convolutional layers are used. He et al. (2020) employed auxiliary tasks including center estimation and foreground segmentation to guide the network to learn the intra-object relationship. Deng et al. (2021) proposed voxel RoI pooling to directly extract RoI features from coarse voxels. 2) *Point-based 3D detectors* consume the raw 3D point clouds directly and generate predictions based on (down-sampled) points. Shi et al. (2019) presented a strong point-based feature extractor and generated high-quality proposals on foreground points. 3DSSD (Yang et al., 2020) introduced a new sampling strategy as a supplement to D-FPS, namely F-FPS, to preserve more foreground points within target objects. It also built an anchor-free regression head to predict 3D bounding boxes based on representative points. Zhang et al. (2022) and Chen et al. (2022) optimized the down-sampling strategies with semantic information to preserve foreground points as much as possible. Shi et al. (2020b) proposed to encode the point cloud efficiently in a fixed-radius near-neighbor graph, and predict boxes of object that each vertex in the graph belongs to. Besides, PV-RCNN (Shi et al., 2020a) integrated the multi-scale voxel-based feature representation and point-based features containing accurate location information. While existing works mainly focused on improving the detection accuracy and efficiency of detectors, this work pays attention to the robustness against adversarial attacks.

2.2 Adversarial Attacks on 2D Images

Szegedy et al. (2013) first pointed out that the neural network is susceptible to carefully designed adversarial per-

turbations. An adversarial example that is similar to original data can successfully fool the neural networks to output wrong predictions. The community has expressed concern about the vulnerability of deep learning models and many works have been proposed to search for effective adversarial attacks and possible defense strategies. Goodfellow et al. (2014) proposed the fast gradient method, which uses the gradient calculated by the loss with respect to the image. Kurakin et al. (2018) further extended FGM to an iterative approach (I-FGM), which leads to a higher success rate of attack than basic FGM. In order to stabilize update directions and escape from local maxima, MI-FGM (Dong et al., 2018) introduced a momentum term into iterative process. The projected gradient descent (PGD) (Madry et al., 2018) is similar to MI-FGM except for random initialization of perturbation at the beginning of iteration. Carlini and Wagner (2017) proposed optimization-based C&W attack that finds the closest adversarial example to the original example based on three norm distances. Besides, there are some studies of physically realizable adversarial examples instead of only dealing with collected 2D image data (Hu et al., 2022b; Cheng et al., 2022).

Defense on Adversarial Attack. Against adversarial attacks, numerous defense methods have been proposed. Adversarial training (Goodfellow et al., 2014; Herrmann et al., 2022) is a widely investigated and effective defense method. It enables training a robust model from scratch on training data augmented with adversarial examples. Despite the brought improvement in tasks of image domain, the adversarial training is more time-consuming than training on clean data and takes more epochs to fit adversarial examples (Tramèr et al., 2018). Another way of defense is to perform certain transformations on the adversarial examples and send the transformed input to models. Dziugaite et al. (2016) and Guo et al. (2018) proposed to preprocess images with JPEG compression to mitigate the effect of adversarial perturbation. Xu et al. (2017) enhance the robustness of neural network by reducing the color bit depth of each pixel and spatial smoothing. Osadchy et al. (2017) employed a set of filters, such as the median filter, average filter, and Gaussian low-pass filter, to remove the adversarial noise. Li et al. (2019) added random noise to pixels of adversarial examples to eliminate the effects of adversarial perturbations.

2.3 Adversarial Attacks on 3D Point Clouds

Following previous studies in the image domain, numerous works on adversarial attacks and robustness have been proposed in 3D vision field. Existing 3D adversarial attacks can be roughly classified into three categories: shifting points (Xiang et al., 2019), adding new points (Liu et al., 2020), dropping points (Zheng et al., 2019; Wicker and

Kwiatkowska, 2019). Xiang et al. (2019) firstly proposed 3D adversarial attacks, including adversarial point perturbation, adversarial point generation and adversarial objects generation, against 3D learning models and show effectiveness on attacking PointNet (Qi et al., 2017). Wen et al. (2020) further considered the local consistency of curvatures between the surface of clean input and adversarial examples. Liu et al. (2019) extended FGSM method to generating 3D adversarial examples using triangular mesh constrained with L_∞ norm. Tsai et al. (2020) applied C&W attack (Carlini and Wagner, 2017) with incorporated KNN distance as extra constraint on perturbation. Hamdi et al. (2020) utilized auto-encoders with a novel data adversarial loss to generate network-transferable perturbations. In order to maintain the geometric smoothness, Liu and Hu (2022) suggested limiting point-wise perturbations along the normal direction within a strictly bounded width. Liu et al. (2020) verified adding simple features into original point cloud can generate adversarial point clouds. Zheng et al. (2019) constructed a saliency map and realized attacking models by dropping out the critical points. Typical defense methods in point cloud fields include simple random sampling (Jia et al., 2021), upsampling after denoising (Zhou et al., 2019), gather vector (Dong et al., 2020), provable defense (Liu et al., 2021), adversarial training (Sun et al., 2021; Liu et al., 2019).

Adversarial Attacks on LiDAR-based Detectors. Studies for adversarial attacks on 3D object detection have been scarce so far. Tu et al. (2020) and Abdelfattah et al. (2021) generated adversarial examples by placing adversarial objects on the rooftop of target vehicles, the successful attack of which can be attributed to the lack of relevant training data and mitigated by data augmentation. Tu et al. (2021) learned an adversarial textured mesh in a differentiable manner to attack any multi-sensor 3D detectors by rendering the adversarial mesh into both LiDAR and image inputs. Sun et al. (2020a) constructed a class of spoofing attacks by injecting a small number of spoofed LiDAR points and achieved high success rates on target models. Lehner et al. (2022) proposed to achieve stronger domain generalization ability of detectors by a novel data augmentation that adversarially deforms point cloud of objects along the ray.

3 Adversarial Attacks

In this section, we present the methods for producing adversarial examples to attack LiDAR-based detectors. Let $\mathbf{X} = \{\mathbf{p}_i | i = 1, 2, \dots, N\}$ denote the input point cloud, where N is the number of points, and each point $\mathbf{p}_i \in \mathbb{R}^3$ is characterized with its 3D coordinates (x_p, y_p, z_p) (other properties of points like intensity and elongation are not considered temporarily). Denote by $\mathcal{G} = \{\mathbf{B}_j\}$ the ground-truth 3D bounding boxes for point cloud \mathbf{X} , where $\mathbf{B}_j = (x_j, y_j, z_j, w_j, l_j, h_j, r_j, c_j) \in \mathbb{R}^8$ with (w_j, l_j, h_j) being

the size of the box and (x_j, y_j, z_j) the coordinates of the box center, and r_j the orientation angle.

The objective of adversarial attacks is to modify points of \mathbf{X} , producing the adversarial example \mathbf{X}_a , which could fool deep detectors to output wrong detection results. Such a procedure can be easily reproduced in reality and is also *plausible* even without the presence of the malicious attacker, since there may exist inevitable range errors of the LiDAR sensor, low reflectivity of lasers on black objects, extra objects appear possibly in the scene, and so on. We extend three kinds of adversarial attack methods widely explored in point cloud field (Xiang et al., 2019; Zheng et al., 2019) to LiDAR-based 3D object detection. To make the paper self-contained, we present the generation algorithms of adversarial examples targeting 3D object detection in detail in the rest of this section. Particularly, we discuss the limitation of point perturbation attacks when applied to voxel-based detectors.

3.1 Adversarial Point Perturbation

In perturbation attacks, we derive the adversarial example \mathbf{X}_a by shifting the 3D coordinates of raw points. Specifically, the adversarial perturbation of coordinates can be represented as $\delta = \{\delta_i \in \mathbb{R}^3 | i = 1, \dots, N\}$, and thus, $\mathbf{X}_a = \{\mathbf{p}'_i := \mathbf{p}_i + \delta_i | i = 1, \dots, N\}$. We adopt the non-targeted attack that the adversary does not have a specific target of bounding boxes, but just manipulates the prediction of detector on \mathbf{X}_a to be different from the ground-truth labels. The problem can be further formulated as a gradient-based optimization algorithm:

$$\min J(\mathbf{X}_a, \mathcal{G}) = -L_{det}(\mathbf{X}_a, \mathcal{G}) + \lambda \mathcal{D}(\mathbf{X}, \mathbf{X}_a), \quad (1)$$

where $L_{det}(\cdot)$ is the detection loss, $\mathcal{D}(\cdot)$ is the distance function measuring the magnitude of perturbation δ , and the non-negative parameter λ balances the two terms. As the correspondence between \mathbf{X} and \mathbf{X}_a is known, we simply use the ℓ_2 norm as the distance metric, denoted as \mathcal{D}_{L_2} , to restrain the magnitude of perturbation. Then we can get the gradient of J with respect to \mathbf{X}_a via backpropagation:

$$\nabla_{\mathbf{X}_a} J(\mathbf{X}_a, \mathcal{G}) = \frac{\partial(J(\mathbf{X}_a, \mathcal{G}))}{\partial \mathbf{X}_a}, \quad (2)$$

Taking the iterative fast gradient method (I-FGM) (Kurakin et al., 2018) as an example, we can obtain the adversarial example as:

$$\mathbf{X}_a^0 = \mathbf{X}, \quad \mathbf{X}_a^{t+1} = \text{Clip}_{\mathbf{X}, \epsilon} \left\{ \mathbf{X}_a^t - \alpha \frac{\nabla_{\mathbf{X}_a^t} J(\mathbf{X}_a^t, \mathcal{G})}{\|\nabla_{\mathbf{X}_a^t} J(\mathbf{X}_a^t, \mathcal{G})\|_2} \right\}, \quad (3)$$

where \mathbf{X}_a^t denotes the adversarial example after t iterations, α is the step size, and $\text{Clip}_{\mathbf{X}, \epsilon}\{\mathbf{X}'(i)\}$ is the function performing point-wise clipping of point cloud $\hat{\mathbf{X}}$, defined as:

$$\text{Clip}_{\mathbf{X}, \epsilon}\{\hat{\mathbf{X}}(i)\} = \begin{cases} \hat{p}_i, & \|\hat{p}_i - p_i\| \leq \epsilon \\ p_i + \epsilon \frac{\hat{p}_i - p_i}{\|\hat{p}_i - p_i\|}, & \|\hat{p}_i - p_i\| > \epsilon \end{cases} \quad (4)$$

so the maximum shift distance of each point (ℓ_2 norm of the perturbation) is limited by parameter ϵ . The I-FGM update rule can also be replaced with MI-FGM (Dong et al., 2018), PGD (Madry et al., 2018) or degraded to FGM (Goodfellow et al., 2014).

Attacks on voxel-based detectors. Different from point-based detectors directly consuming raw point clouds, voxel-based methods first convert the point cloud to a regular volumetric representation before applying 3D convolution. Most implementations of state-of-the-art methods initialize the voxel features with mean voxel feature extraction (mean-VFE): denote $\mathbf{V} = p_i, i = 1, 2, \dots, N_{\mathbf{V}}$ as a non-empty voxel containing $N_{\mathbf{V}}$ points, the feature of voxel initialized via:

$$f_{\mathbf{V}} = \frac{1}{N_{\mathbf{V}}} \sum_{p_i \in \mathbf{V}} p_i, \quad (5)$$

then $f_{\mathbf{V}}$ is commonly fed in a sparse convolution network. So according to the rule of backpropagation, when generating adversarial examples of point perturbation attack, each point in voxel \mathbf{V} shares the same gradient and subsequently same perturbation. The attack is less effective since it does not provide distinct perturbation for each point. Moreover, though gradient-based adversarial attacks have shown generalization on various tasks in the image domain, they may encounter a *dilemma* when employed in voxel-based detectors. While the location of grid is fixed and only value of the pixel is perturbed when attacking image-based task, the voxel that point belongs to may change after point perturbation attack since the coordinates of the point change. If we perform re-voxelization on the perturbed point cloud, the imposed perturbation on points may not work for new voxel representation. On the other hand, the sparse 3D convolution is performed on voxel-based representation based on not only the value of voxels but also the location of voxels (Yan et al., 2018). If we do not conduct re-voxelization, the *location* of voxel \mathbf{V} , which also reflects the geometry information of the object and can be used as a basis for detection, is not affected by attacks though the *value* of \mathbf{V} is perturbed. The above two issues are more serious when the voxel size is set smaller, since there are more points that share the same gradient in a single voxel and the perturbed point is more likely to be beyond the boundary of original voxel it belongs to. We evaluate the effectiveness of point perturbation attack against voxel-based detectors in Section 6.1.

3.2 Adversarial Point Detachment

In practical scenarios, the obtained point clouds may be sparser due to occlusion, low-reflectivity objects, and extreme weather. Hence, we also present an adversarial setting by removing *critical* points in a similar way to Zheng et al. (2019). For a given point cloud, the magnitude of point-wise gradients reflects the influence of local position disturbance on the detection loss/predictions. Therefore we construct a saliency map with point-wise gradients derived by backpropagation, and remove points according to the saliency map. Specifically, the importance of each point is measured by sum-of-square of the gradients of the loss with respect to the coordinates:

$$s_i = \|\partial L_{det} / \partial p_i\|_2. \quad (6)$$

Then saliency scores $\{s_i\}_{i=1}^N$ of all points form a saliency map. Considering the dependencies between points, we drop the points *iteratively* such the points already removed will not be involved in the current iteration. For a better understanding of the adversarial removed points, we visualize the saliency map and the point detachment process in Fig 2.

3.3 Adversarial Point Attachment

The point attachment-based adversarial attack is implemented by adding new points $\mathbf{Z} = \{z_i \in \mathbb{R}^3 | i = 1, \dots, M\}$ at appropriate locations to \mathbf{X} . To tackle the challenge posed by the large search space of adding points, following Xiang et al. (2019), we adopt an *initialize-and-shift* method. First, we obtain a saliency map via Eq. (6) and consider the region where saliency points are located to be vulnerable. Accordingly, we choose the points with top- K saliency scores as initial points. Then we shift the initial points, which are further incorporated into \mathbf{X} to form an adversarial example, i.e., $\mathbf{X}_a = \mathbf{X} \cup \mathbf{Z}$. The appropriate displacement of initial points can be obtained by solving the optimization problem formulated in Eq. (1). The generation of the adversarial examples follows an iterative training process, guided by the detection loss and constraint of imperceptibility. Particularly, we adopt the Chamfer distance \mathcal{D}_C as the constraint between \mathbf{X}_a and \mathbf{X} :

$$\begin{aligned} \mathcal{D}_C(\mathbf{X}, \mathbf{X}_a) = & \frac{1}{\|\mathbf{X}\|_0} \sum_{p \in \mathbf{X}} \min_{p' \in \mathbf{X}_a} \|p - p'\| \\ & + \frac{1}{\|\mathbf{X}_a\|_0} \sum_{p' \in \mathbf{X}_a} \min_{p \in \mathbf{X}} \|p - p'\|. \end{aligned} \quad (7)$$

Note that only the added points are updated in each iteration described in Eq. (3).

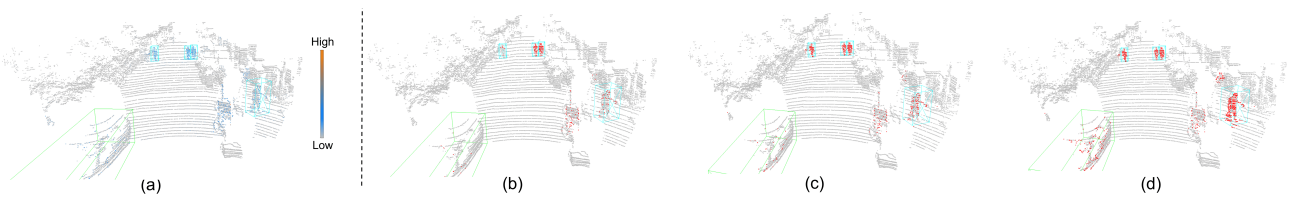


Fig. 2: (a) A saliency map based on the gradient of the loss with respect to the input image. The color of the point represents the size of its gradient. Besides, the GT boxes of cars and pedestrians are shown in green and cyan. (b-d) The illustration of detached points (visualized in red) at 3rd, 7th, 10th iterations, respectively (removing 2% of the point cloud with a total of 10 iterations). Best viewed in color and zoom in for more details.

Table 1: Properties of the LiDAR-based detectors.

Detectors	Representation		Architecture		Params (M)
	Point	Voxel	Point-Voxel	One-stage	
Second		✓		✓	5.33
Voxel-RCNN		✓			7.60
PDV		✓			12.86
PointPillar		✓		✓	4.83
Part-A ²		✓			63.81
PV-RCNN			✓		13.12
3DSSD	✓			✓	2.61
PointRCNN	✓				4.04

4 Defense Mechanisms

Since adversarial examples are produced by introducing unnatural patterns into point clouds, we can apply transformations that remove such patterns to defend the 3D detectors from attacks. In this paper, we study the following 9 defense methods and verify their effectiveness on the adversarial attacks towards 3D object detectors in Section 8.

- **Adversarial training** (Goodfellow et al., 2014), one of the most studied defenses against adversarial attacks, improves the robustness of models against specific attacks by augmenting the training set with corresponding adversarial examples.
- **Simple transformation.** We apply flipping, scaling, and rotation to point clouds as defense methods. The final detection results are derived by applying a contrary transformation to the output of models.
- **Gaussian noise.** The location of each point is perturbed by values randomly drawn from a Gaussian distribution.
- **Quantification.** The coordinates of point cloud data in centimeters are quantized as integers that can mitigate the small variations in coordinates of points.
- **Data augmentation.** We study the effectiveness of part-aware data augmentation (PA-AUG) (Choi et al., 2021) for improving the robustness of detectors against adversarial attacks.
- **Random sampling.** We can obtain a subset of points where each point is chosen randomly with the same probability.

- **KNN-based denoising.** The point clouds are first categorized into several clusters. According to the sigma rule, the point is considered as outlier and removed if it is not within 3 times the standard deviation of distance distribution from the center of cluster (Carrilho et al., 2018).

5 Experiments

5.1 Datasets

The **KITTI** dataset is one of the most commonly used datasets in the outdoor 3D object detection task. Specifically, the KITTI dataset consists of 7481 training samples with annotation of objects in the camera field of vision and 7518 testing samples. The input contains two modalities of point cloud and image. Following prior works (Shi et al., 2020a), we further divide all training samples into two subsets with 3712 and 3769 samples for training and validation respectively. The benchmark further divides the samples into three difficulty levels: easy, moderate, and hard based on the occlusion level, truncation ratio, and object size.

The **Waymo Open Dataset** (Sun et al., 2020b) is a large-scale 3D object detection dataset for autonomous driving. The dataset is collected in diverse scenes and contains 798 sequences (158361 LiDAR frames) for training, 202 sequences (40077 LiDAR frames) for validation, and 150 testing sequences. For each sequence, there are about 200 frames with LiDAR points, multi-view camera images and object annotations in full 360°. The objects are further categorized into two difficulty levels: LEVEL_L1 for objects with more than five observed LiDAR points, and LEVEL_L2 for objects with 1-5 points. The mAP and mAPH (mAP weighted by heading accuracy) are commonly adopted as metrics to evaluate the 3D object detectors.

5.2 Target LiDAR-based Detectors

We consider eight state-of-the-art deep learning-based LiDAR detectors with different structures and properties, in-

Table 2: Ablation of re-voxelization of perturbed point cloud and flipping the direction of perturbation imposed on points for Second detectors.

Attack	Re-voxelization	Flipping Perturbation	ϵ (cm)					
			0.5	1	3	5	7	10
FGM	✓		99.98	99.54	99.39	99.19	98.62	98.44
	✓		99.44	100.50	102.01	103.09	99.82	91.58
		✓	99.09	98.07	96.78	94.15	91.35	83.03
MI-FGM	✓		99.98	99.54	99.39	99.21	98.63	98.40
	✓		99.44	100.53	102.27	102.48	100.73	92.00
		✓	98.96	98.00	96.75	94.25	91.81	82.40
PGD	✓		99.98	99.60	99.47	99.35	99.20	98.63
	✓		99.63	101.26	99.71	101.78	103.19	93.77
		✓	99.58	97.67	95.12	91.95	85.74	70.80

cluding Second (Yan et al., 2018), Voxel-RCNN (Deng et al., 2021), PDV (Hu et al., 2022a), PointPillar (Lang et al., 2019b), Part-A² (Shi et al., 2020b), PV-RCNN (Shi et al., 2020a), 3DSSD (Yang et al., 2020), PointRCNN (Shi et al., 2019). Table 1 shows their characteristics in terms of the feature representation, network architecture, and the number of model parameters. The goal of all models is to detect 3 types of objects: cars, pedestrians, and cyclists. We use the publicly available code and pre-trained models as much as possible. For methods without available pre-trained models, we retrain the models with default configuration provided by original authors.

5.3 Implementation Details

Adversarial attacks. First, for the point perturbation attack, we obtain the adversarial examples with FGM, MI-FGM, and PGD described in Section 3. For the iterative attacks, the number of iterations is set to 40, and the step size α is set to $\epsilon/30$. We evaluate the point perturbation attack when l_2 norm of perturbation ϵ is set to each value in {0.5, 1, 3, 5, 7, 10}cm. *Second*, we evaluate the point detachment attack when setting the ratio of detached points to each value from {0.001, 0.003, 0.005, 0.007, 0.01, 0.02}, and the points are gradually detached in total 10 iterations. Thirdly, 164 and 500 points are attached to the raw point clouds in point attachment attack for KITTI and Waymo datasets respectively, while the l_2 norm of perturbation ϵ on *attached* points take values in {0.05, 0.1, 0.3, 0.5, 0.7, 1}m. Our adversarial attack methods are implemented with Pytorch framework (Paszke et al., 2019).

Robustness measurement. As the mAP value of different 3D detectors varies, we adopt the relative metric called mAP ratio, i.e., the ratio of IoU on adversarial examples to that on clean point cloud over the whole validation set. The models that achieve a higher mAP ratio under adversarial attacks are considered more robust. We measure the robustness (mAP ratio) of detectors against our presented adversarial attacks.

We report the value of mAP ratio on both KITTI and Waymo datasets.

Perceptibility measurement. We expect the adversarial examples to be imperceptible, i.e., they should be close to the corresponding raw point clouds. Therefore, we predominantly use the Chamfer Distance (CD) to measure the deviation of adversarial points \mathbf{X}_a to the raw point cloud \mathbf{X} (as described in Eq. (2)).

6 Evaluation of Adversarial Attacks

In this section, we assess the effectiveness of the different types of attacks and the robustness of different detectors against adversarial attacks.

6.1 Attacking Voxel-based Detectors

As discussed in Section 3.1, the point perturbation attack has two inherent limitations when applied to voxel-based detectors. Here, we experimentally explore the effectiveness of the point perturbation attack on voxel-based detectors, as well as the influence of the re-voxelization operation and voxel size on attack performance. From the quantitative results listed in Table 2, we have the following observations:

- the point perturbation attack can hardly mislead the voxel-based detectors if the perturbed points are not re-voxelized. Without re-voxelization, the mAP ratios of Second are as high as 98.44%, 98.40%, 98.63% under FGM, MI-FGM, PGD-based point perturbation, respectively. The results support our claim in Section 3.1, i.e., only adding perturbation on the values of the voxel representation without changing its location at the same time results in low attack performance;
- after applying re-voxelization of the perturbed point cloud, the performance of detectors even increases slightly. For example, the mAP ratio of Second is 103.19% on the KITTI dataset for the PGD-based perturbation attack

Table 3: Ablation of flipping the direction of perturbation when applying point perturbation attack ($\epsilon=10\text{cm}$) on Second detector with input voxel representation with different sizes.

Voxel Size	Flipped Perturbation	FGM	MI-FGM	PGD
[0.05, 0.05, 0.1]	✓	91.58 83.03	92.00 82.40	93.77 70.80
[0.10, 0.10, 0.2]	✓	105.73 83.79	104.30 83.46	101.10 74.23
[0.16, 0.16, 0.4]	✓	94.32 96.84	94.29 94.04	93.61 97.37
[0.20, 0.20, 0.4]	✓	88.64 103.23	91.65 104.16	89.55 101.78

with $\epsilon=7\text{cm}$. The reason is that the re-voxelization operation disrupts the unnatural patterns introduced by adversarial attacks and yields stronger robustness;

- since the common attacks with the re-voxelization operation abnormally improve model performance, empirically, we further try to change the direction of perturbation, i.e., the sign of $\nabla_{\mathbf{x}_a^t} J(\mathbf{X}_a^t, \mathcal{G})$ in Eq. (3), which is performed on the coordinates of points before re-voxelization. We can observe that attacks with flipped perturbation can effectively decrease the performance of detectors for all FGM, MI-FGM, and PGD-based point perturbation attacks with various ϵ values.

Then we further explore the influence of voxel size of input on the robustness of voxel-based detectors. We can make two intriguing observations from Table 3: (1) The point perturbation attacks with re-voxelization but no flipping perturbation is more effective on detectors with larger voxel-based input. It supports the speculation that re-voxelization mitigates the patterns introduced by adversarial attacks such that the attack is more effective when the voxel size is larger and points are less possible to be beyond the scope of voxels they originally belong to. (2) On the other hand, when the voxel size is set larger and the point perturbation attack is less sensitive to the re-voxelization, flipping the direction of perturbation in Eq. (3) leads to the increase of target in Eq. (1) and better detection performance on the adversarial examples. We also observe similar results on other voxel-based detectors including Voxel-RCNN, Part-A². Since we do not change the default configuration including voxel size of these detectors, we employ re-voxelization and flipping perturbation operation for them in the following sections to pursue better attack performance.

6.2 Evaluation of Adversarial Point Perturbation Attack

Figure 3 shows the robustness of several state-of-the-art detectors on the KITTI benchmark. From the reported results, we have the following observations. (1) In general, the most

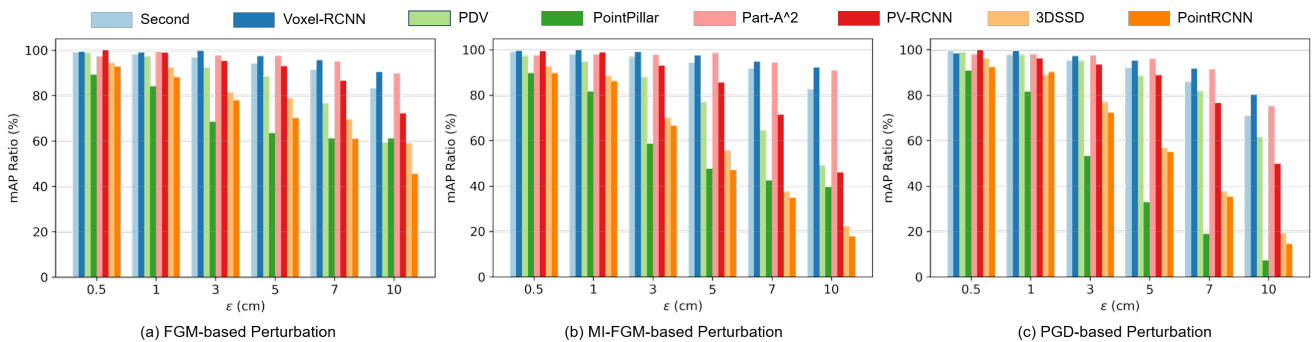


Fig. 3: Adversarial robustness of detectors against point perturbation attack with different ϵ values on KITTI dataset.

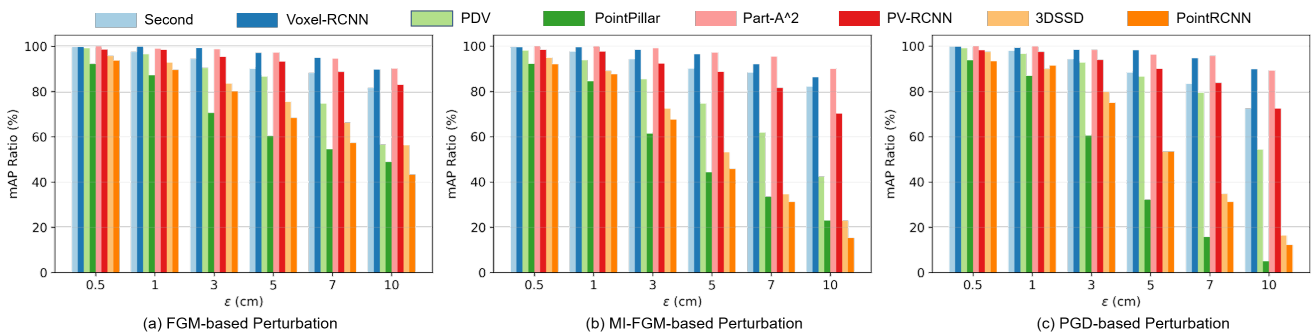


Fig. 4: Adversarial robustness of detectors against point perturbation attack with different ϵ values on Waymo dataset.

widely used gradient-based attack adopted for perturbation of point cloud can successfully disrupt the 3D detectors. For example, the PGD-based point perturbation attack successfully reduces the mAP of the PointPillar from 67.22% to 4.89% (i.e., the mAP ratio is 72.82%) under the PGD-based perturbation attack with ϵ of 10cm. (2) Most of the detectors achieve a similar mAP ratio under the setting of smaller ϵ , while detectors show different levels of robustness against point perturbation attack when the magnitude

of the perturbation is larger. (3) As ϵ increases, the performance degradation of detectors becomes severe against three types of gradient-guided adversarial attacks. The iterative attack (MI-FGM and PGD) is more effective than the single-step attack (FGM). On the most effective PGD-based attack (Figure 3(c)), the robustness of models varies significantly—PointPillar, 3DSSD, and PointRCNN are more vulnerable to adversarial examples. Besides, we also test the robustness of detectors on the waymo validation set as

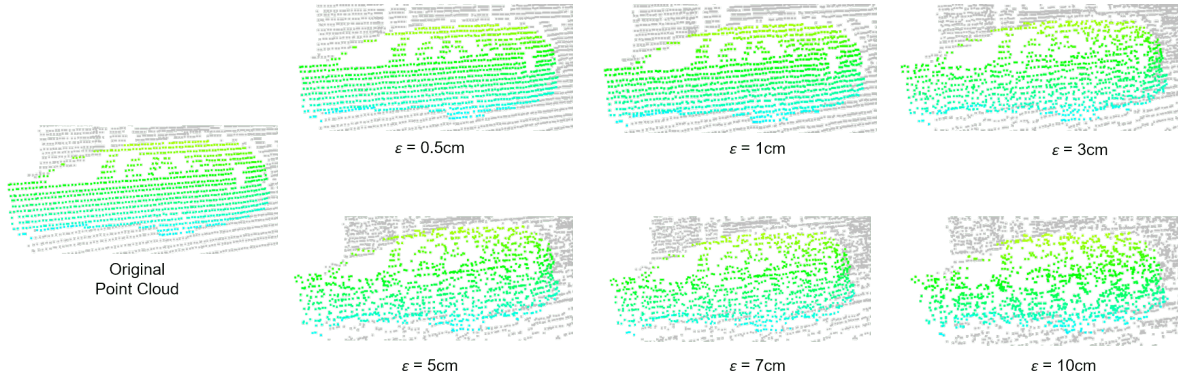


Fig. 5: Illustration of point clouds that belong to a typical car under point perturbation attacks with different ϵ values. It can be observed that the shape of car is still preserved under adversarial attack.



Fig. 6: Visual results of three detectors when PGD-based point perturbation attacks with various ϵ values are applied. The predicted bounding boxes of car, pedestrian, and cyclist are visualized in green, cyan, and yellow, respectively. The ground-truth bounding boxes are visualized in red. Best viewed in color and zoom in for more details.

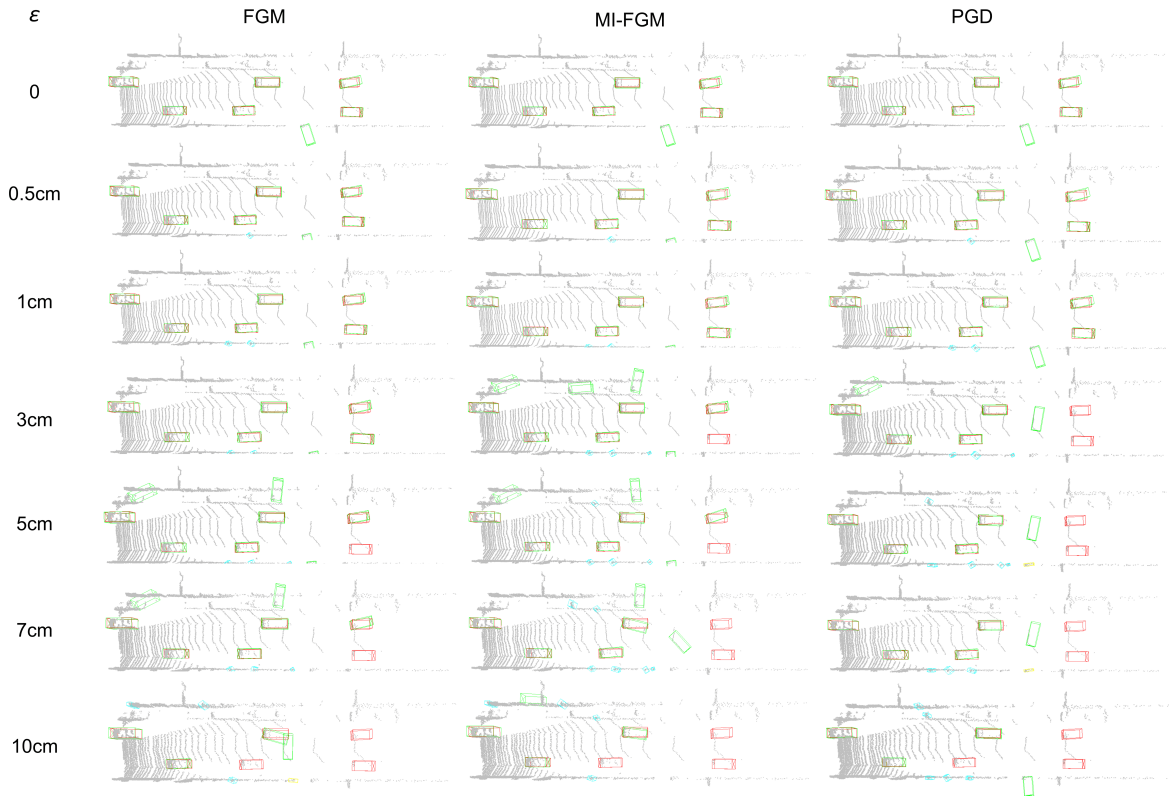


Fig. 7: Comparison of different types of point perturbation attacks applied on PointRCNN. The predicted bounding boxes of **car**, **pedestrian**, and **cyclist** are visualized in green, cyan, and yellow, respectively. The **ground-truth** bounding boxes are visualized in red. Best viewed in color and zoom in for more details.

shown in Figure 4. The detectors show similar relative rankings of robustness, which proves that the robustness is highly correlated with the structure and properties of the detector. We detailedly discuss the robustness of different networks in Section 6.6.

Qualitative results. Figure 5 visualizes the deformation of point cloud under point perturbation attack with various ϵ values. Figure 6 present the detection results under PGD-based point perturbation attack with different ϵ values. We can observe the detector achieves worse detection results with more false-positive boxes and objects not detected when the ϵ value of perturbation increases. On the other hand, the adversarial attack shows the strongest attack performance on the point-based detectors, i.e., PointRCNN. Figure 7 shows the detection results of PointRCNN under different types of point perturbation attacks, we can observe that the PGD-based attack achieves the strongest attack performance.

6.3 Evaluation of Adversarial Point Detachment Attack

Figure 8 compares the performance of detectors with respect to different ratios of dropped points when the point detachment attack is applied. Intuitively, the performance decreases

when the ratio of dropped points increases. For instance, the performance of PDV dropped by 51.87% (i.e., 48.13% mAP ratio) under point detachment attack with only 2% points dropped. The low performance of the detectors under adversarial point detachment attack is understandable since it is hard to predict 3D bounding boxes with seven degrees of freedom based on fewer points. For the adversarial detachment attack, the margin between the most and least robust network is smaller compared to that of point perturbation attack. And the models including Second, 3DSSD, and PointRCNN are clearly less vulnerable to the point detachment attack compared with the point perturbation attack. We further evaluate nine defense strategies against point detachment attack in Section 8.

6.4 Evaluation of Adversarial Point Attachment Attack

Figure 9 shows the performance of detectors against the point attachment attack with respect to different ϵ values. Curiously, the performance of detectors does not always decrease with the increase of ϵ (i.e., the more intense disturbance). The reason may be that under larger ϵ , the attached points have a larger displacement and thus have fewer effects on the critical

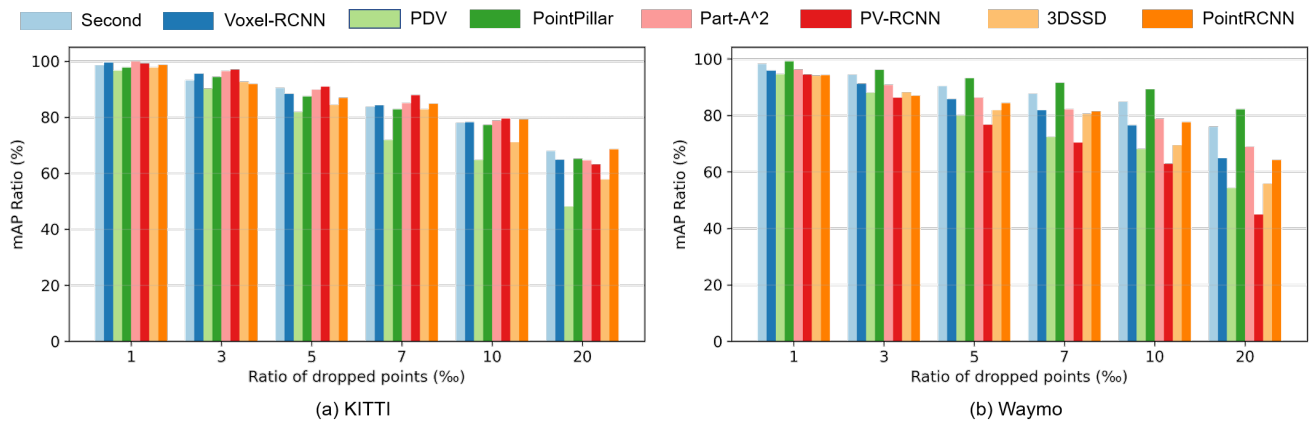


Fig. 8: Adversarial robustness of detectors against point detachment attack with different ratios of detached points on KITTI and Waymo datasets.

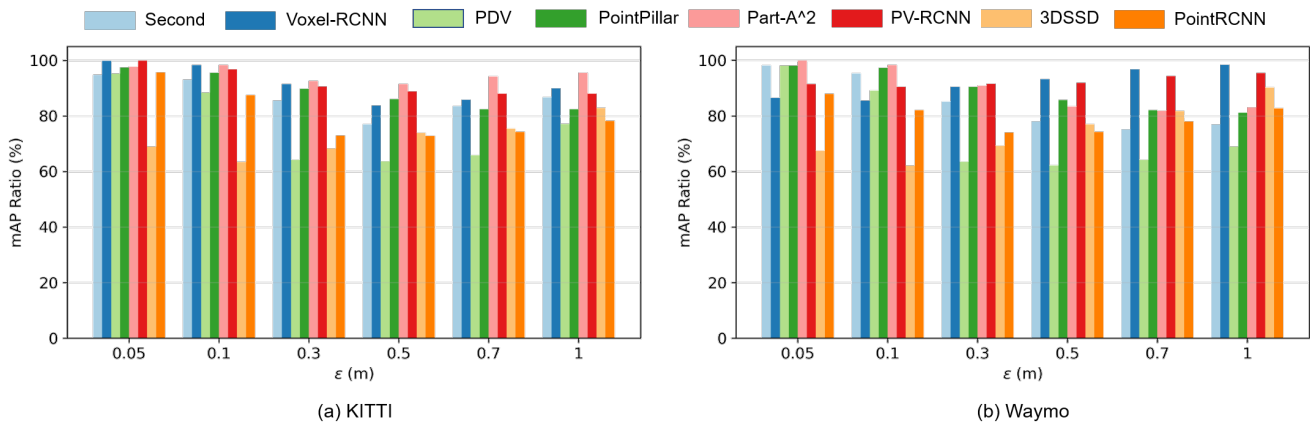


Fig. 9: Adversarial robustness of detectors against point attachment attack with different values of ϵ for attached points. The number of attached points is set to 164 and 500 on KITTI and Waymo datasets, respectively.

points. Besides, we can observe that PDV is obviously vulnerable under point attachment and detachment attacks. The reason for vulnerability of PDV may be its own specific characteristics of leveraging features of point density, as well as the density confidence prediction module which refines the confidence predictions of proposals with the *number* of LiDAR points within the proposal as additional features (Hu et al., 2022a). Compared with the performance of point perturbation attack, the results reported in Figure 9 imply that attacking vulnerable regions by adding new points is less malignant than directly applying perturbation to original point cloud.

6.5 Attack Performance Versus Perceptibility

We report the performance of adversarial attacks towards different detectors and the perceptibility of adversarial examples in Table 4, where it can be observed that the point pertur-

Table 4: Performance of three attacks towards different detectors and the corresponding perceptibility of adversarial examples. The mAP ratio (%) is reported.

Detectors	Perturbation		Detachment		Attachment	
	CD	mAP Ratio	CD	mAP Ratio	CD	mAP Ratio
Second	0.0125	70.80	0.0260	67.92	0.0004	85.50
Voxel-RCNN	0.0124	80.24	0.0107	64.84	0.0004	91.45
PDV	0.0125	61.61	0.0267	48.13	0.0005	64.14
PointPillar	0.0125	7.28	0.1116	65.14	0.0001	89.80
Part-A ²	0.0124	75.11	0.0074	64.54	0.0004	92.58
PV-RCNN	0.0125	49.80	0.0183	63.21	0.0004	90.56
3DSSD	0.0129	19.07	0.0222	57.75	0.0005	68.27
PointRCNN	0.0142	14.44	0.0100	68.49	0.0005	72.86
Average	0.0127	47.29	0.0291	62.50	0.0004	81.89

Note: ϵ is set to 10cm and 30cm for point perturbation and attachment attack, respectively. The ratio of dropped points is set to 0.02 for point detachment attack.

bation attack achieves the best attack performance while the perceptibility of its corresponding adversarial examples is

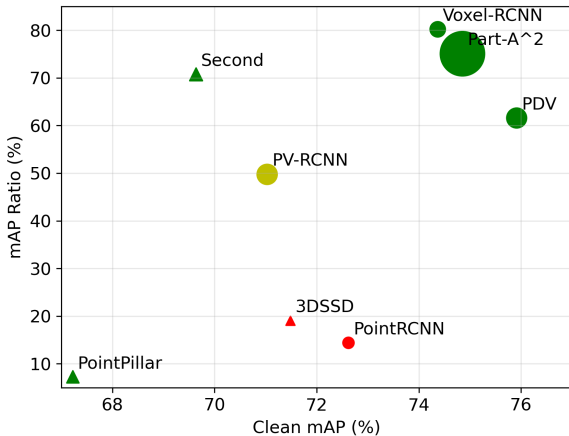


Fig. 10: The mAP ratio of detectors under the PGD-based point perturbation attack with $\epsilon=10\text{cm}$ on the KITTI dataset. We use red, green, and yellow to denote the voxel-based, point-based, and point-voxel-based detectors, respectively. Triangle and circle denote the one-stage and two-stage detectors respectively. The larger the marker, the larger the network size.

lower than the point detachment attack. Although the adversarial examples generated by the point attachment attack is least perceptible, the attack is far less effective than point perturbation and detachment attacks.

With the constraint of ϵ in Eq. (4) to limit the magnitude of perturbation, the CD of adversarial examples is similar among different detectors under point perturbation attack.

Besides, we find that the effectiveness of the attack is not positively related to the CD between adversarial examples and raw point cloud. For example, for PointPillar, the attack performance (7.28% mAP ratio) under point perturbation attack is better than that of the point detachment attack (65.14%), though the CD metric of the former is smaller.

6.6 The Robustness of Different Networks

The point perturbation-based attack has been demonstrated to be the most effective among the three types of attacks. We further illustrate the correlation between the mAP on clean data and robustness to the perturbation attack in Figure 10, where we have the following observations:

- First, we can find voxel-based methods generally achieve higher mAP ratios against the adversarial perturbation attack than the point-based detectors. Both point-based 3DSSD and PointRCNN show much lower mAP ratios than voxel-based detectors except for PointPillar. However, we can not simply conclude that voxel-based detectors are more robust. As stated in Section 3.1, there are

two limitations when applying point perturbation attack against voxel-based detectors, which make the adversarial examples generated from voxel-based method less malignant. We further evaluate the robustness of detectors under black-box (cross-model and cross-task) attack in Section 7.

- PDV achieves the highest performance on the clean point cloud input but it shows worse robustness compared with the simple Second detector. It indicates that detection accuracy on clean input and robustness are not equivalent, models with higher accuracy may be less resistant to adversarial attacks. The results are inconsistent with the observed correlation between accuracy on clean data and robustness in the image-based tasks (Szegedy et al., 2013).
- It can be observed that the PointPillar shows the lowest mAP ratio among all 3D object detectors, which suggests its potential limitations. The phenomenon can be attributed to the specific characteristics of PointPillar, including a large size of input voxel ([0.16, 0.16, 4]) and Pillar feature network (Lang et al., 2019a).
- Probably because of point-voxel representation introduced by the multi-scale point-voxel integration strategy, PV-RCNN achieves a lower mAP ratio compared with voxel-based two-stage detectors like Voxel-RCNN and Part-A².
- Compared with feature representation and other properties, model size does not significantly affect the robustness against adversarial attacks. For example, Second and PointRCNN with similar sizes of parameters (5.33M vs 4.04M) show largely different robustness. This phenomenon indicates that some observations made in the context of image classification, such as too large or too small models leading to poor robustness (Kurakin et al., 2017), cannot be directly transferred to the task of 3D object detection.
- Compared with feature representation, whether the model is a one-stage or two-stage structure does not significantly affect the robustness.

7 Transferability Evaluation

In the preceding section, we assessed the effectiveness of the source attack, in which the adversarial examples are obtained with available models and known ground-truth bounding boxes. Since there may be no direct access to the target detectors, we also study the potential vulnerability of detectors under black-box attacks. Except for the source attack assessed, we further study the effectiveness of attacks in three settings in this section:

- Cross-model attack: We obtain the adversarial examples learned from another model to fool the target detectors.

Table 5: Transferability of adversarial examples for *point perturbation attack* generated from source models and evaluated on target models. The gray diagonals denote white-box attacks, and off-diagonals show transfer (black box) attacks. The most effective black-box attack for each target detector is bold.

mAP Ratio (%)		Source Model							
		Second	Voxel-RCNN	PDV	PointPillar	Part-A ²	PV-RCNN	3DSSD	PointRCNN
Target Model	Second	70.80	77.22	65.55	65.65	77.36	64.99	54.04	49.77
	Voxel-RCNN	85.06	80.24	71.64	71.20	86.90	72.78	67.26	58.47
	PDV	83.69	86.90	61.61	74.05	86.35	75.50	66.80	59.69
	PointPillar	92.64	93.17	84.00	7.28	95.44	88.37	80.48	81.29
	Part-A ²	80.65	80.40	63.32	63.62	75.11	65.73	58.96	52.59
	PV-RCNN	75.09	76.55	59.92	63.22	75.85	47.96	58.29	50.65
	3DSSD	87.32	85.46	73.70	77.53	88.55	73.55	19.07	55.52
	PointRCNN	71.78	70.95	59.23	64.55	71.39	59.79	56.67	14.44

Table 6: Transferability of adversarial examples for *point detachment attack* generated from source models and evaluated on target models. The gray diagonals denote white-box attacks, and off-diagonals show transfer (black box) attacks. The most effective black-box attack for each target detector is bold.

mAP Ratio (%)		Source Model							
		Second	Voxel-RCNN	PDV	PointPillar	Part-A ²	PV-RCNN	3DSSD	PointRCNN
Target Model	Second	67.92	63.99	47.90	62.06	64.63	59.91	55.40	68.71
	Voxel-RCNN	68.39	64.84	49.47	63.48	65.34	62.27	54.02	67.98
	PDV	65.49	64.01	48.13	63.26	64.95	59.19	53.87	67.78
	PointPillar	67.79	63.63	49.42	65.14	63.93	57.04	54.77	64.73
	Part-A ²	67.58	64.08	49.11	60.47	64.54	61.25	53.60	70.12
	PV-RCNN	69.66	65.31	50.78	64.25	66.92	63.21	55.43	71.26
	3DSSD	70.19	66.34	53.14	66.75	68.80	59.69	57.75	74.06
	PointRCNN	61.73	58.89	43.85	60.10	60.52	51.60	56.33	68.49

Table 7: Transferability of adversarial examples for *point attachment attack* generated from source models and evaluated on target models. The gray diagonals denote white-box attacks, and off-diagonals show transfer (black box) attacks. The most effective black-box attack for each target detector is bold.

mAP Ratio (%)		Source Model							
		Second	Voxel-RCNN	PDV	PointPillar	Part-A ²	PV-RCNN	3DSSD	PointRCNN
Target Model	Second	85.50	88.87	71.30	94.24	88.77	92.04	86.96	90.21
	Voxel-RCNN	90.55	91.45	72.51	96.31	92.65	93.17	88.68	89.90
	PDV	89.67	90.77	64.14	95.54	91.91	92.03	89.27	90.21
	PointPillar	87.61	87.92	75.51	89.80	91.31	92.79	83.21	84.83
	Part-A ²	91.71	91.15	75.80	94.60	92.58	93.17	92.07	92.09
	PV-RCNN	91.67	93.76	71.51	96.93	92.86	90.56	91.63	94.42
	3DSSD	88.92	86.08	68.30	95.06	91.67	97.43	68.27	96.95
	PointRCNN	78.25	77.49	61.79	88.43	79.56	79.73	87.91	72.86

- Cross-domain attack: The adversarial examples are generated based on detectors that are optimized on another domain, which are used to fool the detectors trained on the target domains.
- Cross-task attack: We use the adversarial examples generated on 3D semantic segmentation tasks to attack the detectors.

The source attack belongs to white-box attacks while the cross-model, cross-domain, and cross-task attacks belong to black-box setting, since the structure and parameters of the targeted 3D detectors are not necessarily available in those attacks.

7.1 Evaluation on Cross-model Attack

Table 5 summarizes the transferability of point perturbation attack for the eight kinds of detectors on the KITTI dataset, where $\epsilon=10\text{cm}$. The results show that the adversarial examples are transferable between different detectors to some extent. As mentioned before, point-based detectors are less robust against point perturbation attacks compared with voxel-based detectors. And we can clearly observe that adversarial examples generated based on PointRCNN or 3DSSD are also effective in attacking other detectors. The detectors including Second, Voxel-RCNN, PDV, and Part-A² achieve lower mAP ratios under the transferred attack than that under source attack when the PointRCNN is used as the source model. As mentioned before, we speculate the reason for the weakness of source attack on the voxel-based detectors is that attacks *default* the voxels that perturbed points belong to unchanged when generating adversarial examples and does not take the re-voxelization of perturbed point cloud into consideration. Although we manage to make the attack effective by ad hoc flipping the direction of perturbation as mentioned in Section 6.1, the generated perturbation is still not as effective as transferred attacks generated based on point-based detectors. As shown in Figure 11, the transferred attack generated from PointRCNN leads to more false positive predictions and objects not detected in the detection results of other models.

Besides, the PointPillar is vulnerable to the point perturbation attack, but neither the transferred attack from PointPillar is effective on other detectors, nor the transferred attack from other detectors can be effective to PointPillar. The reason is the large voxel size and special Pillar feature network adopted in PointPillar are significantly different from the pipeline of other detectors.

Table 6 summarizes the transferability of the point detachment attack generated from different detectors on the KITTI dataset, where the ratio of detached points is set to 2%. The adversarial examples, generated from PDV and 3DSSD which are vulnerable to source attack, show stronger attack performance on other detectors. In general, detectors show

similar robustness against the transferred point detachment attack generated from another detector. Besides, Table 7 summarizes the transferability of point detachment attack generated from different detectors on the KITTI dataset, where the max displacement of attached points ϵ is set to 30cm. We can observe that the transferred point attachment attack generated from PDV, which shows vulnerability to the source attack, are most effective on other detectors. The reason for the vulnerability of PDV compared with other voxel-based detectors may be the adopted Density Confidence Prediction (Hu et al., 2022a), which refines the confidence predictions of proposals with the number of LiDAR points within the proposal as additional features and thus make the pipeline sensitive to point detachment or attachment in the critical regions.

7.2 Evaluation on Cross-task Attack

In this part, we explore whether the adversarial examples generated on 3D semantic segmentation models can transfer to 3D detectors. Specifically, we adopt a PointNet++ structure for the 3D semantic segmentation and obtain adversarial examples following point perturbation attack described in Section 3 and adapted with the loss of 3D semantic segmentation. We conduct experiments under the point perturbation attack instead of point detachment and attachment considering its appropriate balance between performance and perceptibility reported in Table 4.

We summarize the results of cross-task transfer attacks in Table 8. Adversarial examples are generated by FGM, MIFGM, and PGD rule ($\epsilon=10\text{cm}$) on semantic segmentation models and evaluated on state-of-the-art detectors. Generally, the cross-task transfer point perturbation attack is significantly more effective than direct source attack reported in Figure 3 on voxel-based detectors. Specifically, the mAP ratios under source point perturbation attack (PGD-based) of Second, Voxel-RCNN, Part-A² are 70.80%, 80.24%, and 75.11%, respectively, while that under transferred attack from 3D semantic segmentation are 48.09%, 59.95%, and 47.43%. This observation suggests the weakness of source attack for voxel-based detectors again. We can not assume voxel-based detectors are robust just because it has higher mAP ratios under source attack, considering the inherent limitation of source attack as described in Section 6.1. Even so, considering the performance of detectors under source attack, cross-model attack, and cross-task attack, voxel-based detectors are still generally more robust than point-based detectors. Besides, the effectiveness of transferred attack from 3D semantic segmentation task makes sense, as the model adopts point-based representation and backbones like 3DSSD and PointRCNN. BTW, the iterative attacks are still more effective than the single-step attacks in the cross-task attack.

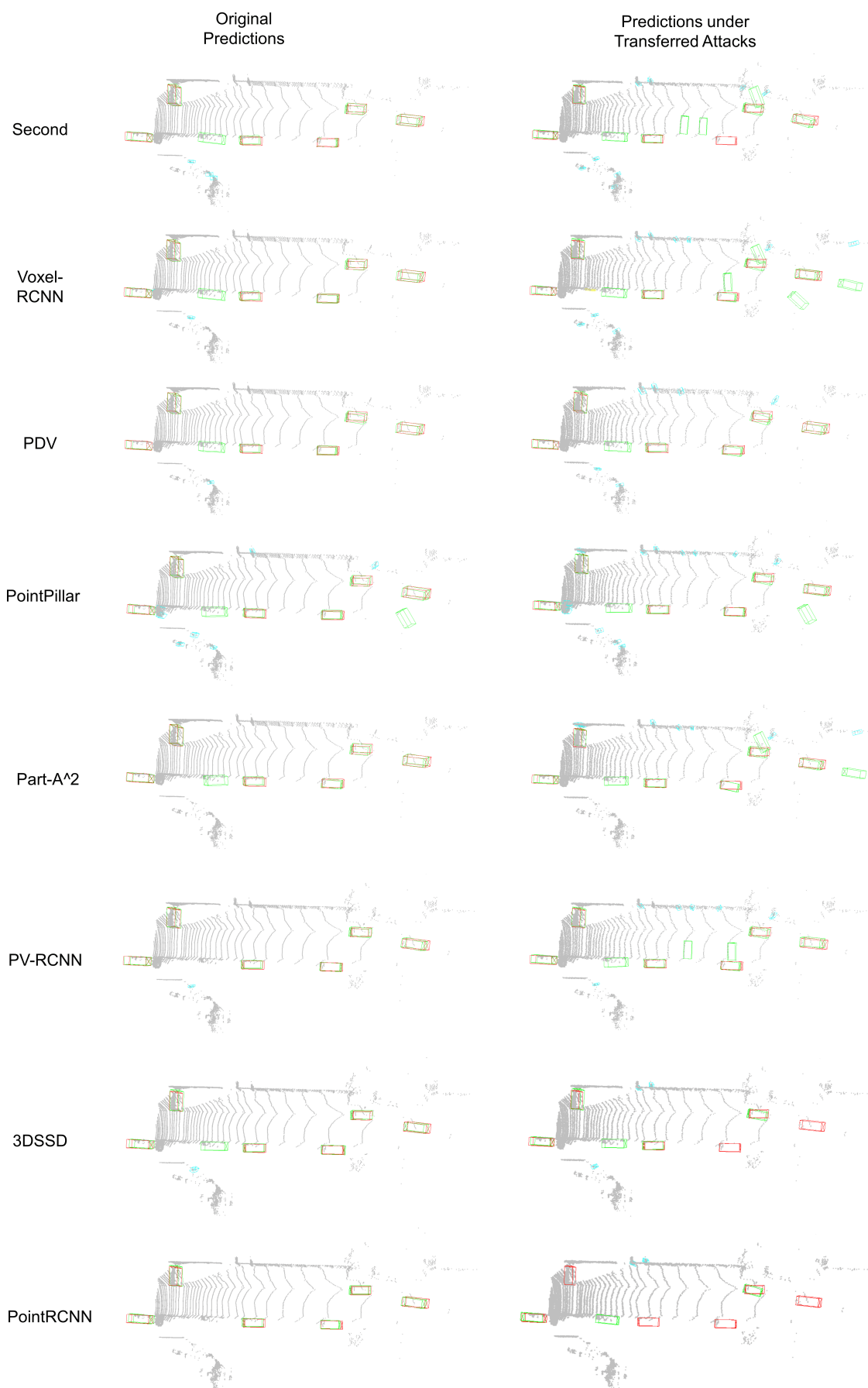


Fig. 11: Detection results of state-of-the-art detectors on clean input and the transferred adversarial examples generated from PointRCNN under point perturbation attack. The predicted bounding boxes of car, pedestrian, and cyclist are visualized in green, cyan, and yellow, respectively. The ground-truth bounding boxes are visualized in red. Best viewed in color and zoom in for more details.

Table 8: Performance of cross-task point perturbation attack that uses perturbation generated from 3D semantic segmentation model to attack 3D object detectors. The mAP ratio is reported.

Attack		Second	Voxel-RCNN	PDV	PointPillar	Part-A ²	PV-RCNN	3DSSD	PointRCNN	Average
Source Attack	FGM	83.03	90.38	59.35	61.09	89.64	72.14	59.05	45.40	70.01
	MI-FGM	82.40	92.20	48.93	39.55	90.79	46.02	22.27	17.76	54.99
	PGD	70.80	80.24	61.61	7.28	75.11	49.80	19.07	14.44	47.29
Cross-task Attack	FGM	59.35	70.77	68.53	86.18	60.62	54.07	69.39	66.70	66.95
	MI-FGM	41.92	54.63	54.97	76.56	44.06	37.68	52.69	51.68	51.77
	PGD	48.09	59.95	61.72	80.23	47.43	43.20	62.15	56.88	57.46

Table 9: Performance of cross-domain point perturbation attack that uses adversarial examples generated from models trained on Waymo to attack target model on KITTI dataset. The cross-domain attack belongs to the black-box attack since it is unnecessary to access the parameters of target model. The mAP ratio (%) is reported.

Attack		Second	Voxel-RCNN	PDV	PointPillar	Part-A ²	PV-RCNN	3DSSD	PointRCNN	Average
Source Attack	FGM	83.03	90.38	59.35	61.09	89.64	72.14	59.05	45.40	70.01
	MI-FGM	82.40	92.20	48.93	39.55	90.79	46.02	22.27	17.76	54.99
	PGD	70.80	80.24	61.61	7.28	75.11	49.80	19.07	14.44	47.29
Cross-domain Attack	FGM	97.69	71.53	75.60	91.08	71.22	85.91	75.18	67.44	79.46
	MI-FGM	98.20	47.80	75.04	93.77	59.75	85.57	44.17	41.68	68.24
	PGD	84.03	54.62	66.34	90.69	64.10	78.12	37.07	40.60	64.45

7.3 Evaluation on Cross-domain Attack

In this part, we explore the effectiveness of cross-domain attacks, where the perturbation is generated from models trained on Waymo dataset *without* having knowledge of data distribution of target domain (KITTI dataset).

As shown in Table 9, the adversarial examples are *transferable* across different domains, though most of transferred perturbation attacks are not as effective as the source attack. Particularly, the cross-domain attack is even more effective than the source attack on Voxel-RCNN and Part-A². And the cross-domain attacks lead to a significant performance decrease on point-based detectors (3DSSD and PointRCNN), which have been verified as vulnerable to the source attacks. How to design an effective cross-domain attack is a meaningful topic and deserves further research in the future.

8 Evaluation of Defenses

8.1 Robustness Conferred by Defense

In this section, we examine the effectiveness of 9 defense methods against three types of attacks for 3D object detection. For the simple transformations including flipping, scaling, rotation, quantification, and random sampling, we apply the transformation to adversarial examples before they are passed through the network.

Table 10 summarizes the robustness of detectors after applying defense methods, where we have the following observations: (1) For the PGD-based point perturbation attack on

KITTI, the adversarial training brings substantial benefits for robustness of most detectors. The improvement makes sense because adversarial training enables the detectors to learn the distribution of perturbation. (2) Simple transformations including flipping, scaling, rotation, and random sampling bring smaller but still sizeable benefits, which demonstrates they could mitigate the unnatural patterns imposed by adversarial attacks on point cloud. (3) Although PA-AUG has been demonstrated to improve the robustness of detectors to corrupted data (Choi et al., 2021), it brings little benefit for the robustness against adversarial attacks since the distribution of corrupted data and adversarial examples could be different. We also provide qualitative results in Figure 12, we can clearly observe that adversarial training significantly improves the robustness of detectors under point perturbation attack.

Table 11 shows the mAP ratios of detectors under point detachment attack when different defense methods are applied. The adversarial training can substantially improve the robustness of some detectors to point detachment attacks. For example, the mAP ratio of PV-RCNN under point detachment attack improves from 61.35% to 67.66% after applying adversarial training. Neither KNN-based denoising nor random sampling improves the mean values of mAP ratios of detectors under point detachment attack, since they further decrease the number of points. And unlike point perturbation attack, the point detachment attack does not impose perturbation on point cloud, so removing points in the two defense methods is not helpful to mitigate the imposed perturbation.

Table 10: Robustness of detectors (mAP ratio) under point perturbation attack after applying 9 defense methods. For each detector, the result of the most effective defense method is bold. Gaussian: add Gaussian noises to coordinates of points. Sample: random sampling. KNN: KNN-based denoising. AT: adversarial training.

Model	Defense										Average
	None	Flip	Scale	Rotate	Quantify	Gaussian	PA-AUG	Sample	KNN	AT	
Second	70.80	73.22	73.97	75.47	69.68	69.42	72.54	71.98	64.76	92.07	73.39
Voxel-RCNN	80.24	82.73	82.10	84.75	83.79	78.95	79.31	84.22	79.61	75.80	81.15
PDV	61.61	68.54	63.09	66.58	62.96	63.44	61.84	62.37	58.95	72.32	64.17
PointPillar	7.28	41.73	52.13	59.52	11.53	14.08	9.79	9.46	9.38	42.52	25.74
Part-A ²	75.11	80.01	78.22	81.57	74.97	78.22	73.83	78.35	75.46	92.30	78.80
PV-RCNN	49.80	51.64	48.38	54.11	47.87	45.58	50.26	56.43	50.82	76.32	53.12
3DSSD	19.07	33.00	19.38	31.56	17.00	22.17	19.69	24.84	24.98	36.76	24.84
PointRCNN	14.44	28.21	15.86	25.44	16.46	16.04	15.78	25.84	18.04	49.63	22.57
Average	47.29	57.38	54.14	59.88	48.03	48.49	47.88	51.69	47.75	67.22	52.97

Table 11: Robustness of detectors (mAP ratio) under point detachment attack after applying 9 defense methods. The ratio of detached points is set to 2%. For each detector, the result of the most effective defense method is bold. Gaussian: add Gaussian noises to coordinates of points. Sample: random sampling. KNN: KNN-based denoising. AT: adversarial training.

Model	Defense										Average
	None	Flip	Scale	Rotate	Quantify	Gaussian	PA-AUG	Sample	KNN	AT	
Second	67.92	66.88	69.33	71.05	69.00	68.29	69.01	68.16	64.73	73.02	68.74
Voxel-RCNN	64.84	66.74	65.58	66.18	66.17	65.51	64.38	65.75	63.73	52.82	64.17
PDV	48.13	48.29	49.19	48.96	48.76	49.34	49.71	47.31	45.84	50.64	48.62
PointPillar	65.14	62.72	65.15	64.47	65.01	64.46	66.70	63.75	63.04	66.37	64.68
Part-A ²	64.54	63.89	66.52	65.52	65.11	64.55	68.74	65.93	62.94	74.88	66.26
PV-RCNN	61.35	63.74	63.20	62.89	61.66	59.77	62.98	59.77	60.65	67.66	62.37
3DSSD	57.75	56.73	57.19	57.47	56.04	57.19	56.01	57.19	56.01	55.11	56.67
PointRCNN	68.49	68.55	70.09	67.71	71.63	68.76	70.35	67.98	69.19	72.19	69.49
Average	62.27	62.19	63.28	63.03	62.92	62.23	63.49	61.98	60.77	64.09	62.63

Table 12: Robustness of detectors (mAP ratio) under point attachment attack after applying 9 defense methods. For each detector, the result of the most effective defense method is bold. The number of attached points is set to 164 on KITTI dataset. Gaussian: add Gaussian noises to coordinates of points. Sample: random sampling. KNN: KNN-based denoising. AT: adversarial training.

Model	Defense										Average
	None	Flip	Scale	Rotate	Quantify	Gaussian	PA-AUG	Sample	KNN	AT	
Second	85.50	92.40	91.29	88.51	85.76	85.18	86.81	85.09	84.19	92.39	87.71
Voxel-RCNN	91.45	88.18	90.40	88.84	89.30	89.26	92.01	88.42	87.59	75.96	88.14
PDV	64.14	78.56	68.86	68.80	64.91	66.35	66.57	68.16	67.28	74.97	68.86
PointPillar	89.80	87.03	93.89	92.45	92.38	90.80	89.95	90.03	88.21	88.01	90.26
Part-A ²	92.58	86.81	94.90	93.56	93.52	91.67	93.41	94.70	92.93	97.33	93.14
PV-RCNN	90.56	87.88	91.58	91.82	87.46	89.47	89.76	90.50	86.70	93.20	89.89
3DSSD	68.27	84.34	77.14	77.85	75.05	75.30	70.48	77.09	75.58	78.90	76.00
PointRCNN	72.86	85.49	92.54	89.01	90.41	88.79	76.68	86.99	86.24	89.59	85.86
Average	81.89	86.33	87.58	86.36	84.85	84.60	82.83	85.12	83.59	86.29	84.98



Fig. 12: Visual results of detectors on adversarial examples generated by point perturbation attack after applying various defenses. The predicted bounding boxes of **car**, **pedestrian**, and **cyclist** are visualized in green, cyan, and yellow, respectively. The **ground-truth** bounding boxes are visualized in red. Best viewed in color and zoom in for more details.

Table 12 shows that appropriate defense methods can increase robustness of detectors under point detachment attack. The transformation makes the adversarial examples less malignant and the adversarial training makes the model more robust against the disturbance of attached points.

8.2 Defense Against Adaptive Attacks

The results reported in Table 10 show simple transformations, including flipping, rotation, scaling, quantification, and

random sampling can make the powerful PGD-based point perturbation attack less malignant. However, the transformation is applied to the generated adversarial examples. So defenses in this way assume that knowledge of used defense mechanisms is not exploited when generating adversarial examples. According to Kerckhoff's principle (Kerckhoffs, 1883), a system should be safe even if all information about it except for the key is publicly available knowledge. So in this section, we further study whether the defense is effective against adaptive attacks.

Table 13: Robustness of detectors (mAP ratio) after applying 7 transformation-based defense methods under *adaptive* point perturbation attack. For each detector, result of the most effective defense method is bold.

Method \ Defense	None	Flip	Scale	Rotate	Quantify	Gaussian	Sample	KNN
Second	70.80	68.01	68.77	70.56	68.63	65.53	66.57	61.43
Voxel-RCNN	80.24	80.82	80.41	80.92	81.27	79.69	81.16	77.98
PDV	61.61	62.06	62.49	61.77	61.82	58.17	62.48	57.02
PointPillar	7.28	8.62	7.71	7.66	7.75	6.83	7.51	7.08
Part-A ²	75.11	77.55	74.37	75.61	76.80	75.80	77.10	77.75
PV-RCNN	49.80	45.83	51.18	49.57	47.74	47.93	50.80	43.46
3DSSD	19.07	16.46	18.89	19.44	19.65	18.67	19.40	14.80
PointRCNN	14.44	17.72	16.23	16.83	17.04	14.35	14.85	14.13

Specifically, we take the transformed point cloud as input when generating adversarial examples. Particularly, for the defense of adding Gaussian noises, we apply Expectation Over Transformation (EOT) (Athalye et al., 2018) to modify the iterative FGM updation (see Eq. 2) to compute the expected gradient over the distribution of imposed Gaussian noises to the input:

$$\mathbf{X}_a^{t+1} = \text{Clip}_{\mathbf{X}, \epsilon} \left\{ \mathbf{X}_a^t - \alpha \mathbb{E}_{t \sim \mathcal{T}} \frac{\nabla_{\mathbf{X}_a} J(t(\mathbf{X}_a), \mathcal{G})}{\|\nabla_{\mathbf{X}_a} J(t(\mathbf{X}_a), \mathcal{G})\|_2} \right\}, \quad (8)$$

where \mathcal{T} is the distribution of imposed Gaussian noises t . In detail, the average value of normalized gradients of multiple transformed point cloud with respect to the loss is computed and used to update the perturbation in each iteration.

We report the detailed results of (PGD-based) adaptive point perturbation attack on the KITTI dataset in Table 13. We can observe none of the various transformations could provide substantial robustness on the adversarial examples generated by adaptive attack, as the mAP ratio of detectors with defense is similar to value under setting without defense. For example, the rotation transformation could increase the mAP ratio of PointPillar from 7.28% to 59.52% under normal attack (see Table 10), but marginally increase mAP ratio to 7.66% as shown in Table 13. The experimental results suggest that adversarial attacks are not affected by input transformation defense if the adopted transformation is known to the attacker. Meanwhile, the defense of adversarial training is still effective since it works by obtaining more robust models instead of performing transformations on input point cloud. Therefore, adversarial training is the promising way to improve robustness of detectors against adversarial attacks and deserves further study.

9 Conclusion

In this paper, we thoroughly investigated the robustness of 3D detectors under three basic adversarial attacks. The extensive experimental results showed that the state-of-the-art

methods are highly vulnerable to the presented adversarial attacks. We carefully analyze the relationship between the robustness and the properties of detectors in detail. We also show transferability of cross-model, cross-task, and cross-domain attacks. Furthermore, we evaluate the effectiveness of nine defense strategies against adversarial attacks, which shows that adversarial training is the promising way to improve robustness of 3D object detectors. The comprehensive evaluation results suggest which state-of-the-art models for 3D object detection should be preferred in safety-critical applications. We believe our observations could facilitate future efforts to improve the robustness and reliability of the 3D object detectors.

Data Availability Statements

The Waymo Open Dataset (Sun et al., 2020b) and KITTI (Geiger et al., 2012) used in this manuscript are deposited in publicly available repositories respectively: <https://waymo.com/open/data/perception> and <http://www.cvlibs.net/datasets/kitti>.

Conflict of Interest

The authors declare that they do not have any commercial or associative interest that represents a conflict of interest in connection with the work submitted.

References

- Abdelfattah M, Yuan K, Wang ZJ, Ward R (2021) Adversarial attacks on camera-lidar models for 3d car detection. In: 2021 IEEE/RSJ International Conference on Intelligent Robots and Systems (IROS), IEEE, pp 2189–2194
- Athalye A, Carlini N, Wagner D (2018) Obfuscated gradients give a false sense of security: Circumventing defenses

- to adversarial examples. In: International Conference on Machine Learning, vol 80, pp 274–283
- Carlini N, Wagner D (2017) Towards evaluating the robustness of neural networks. In: IEEE Symposium on Security and Privacy, Ieee, pp 39–57
- Carrilho A, Galo M, Dos Santos RC (2018) Statistical outlier detection method for airborne lidar data. *International Archives of the Photogrammetry, Remote Sensing & Spatial Information Sciences* 42(1)
- Chen C, Chen Z, Zhang J, Tao D (2022) Sasa: Semantics-augmented set abstraction for point-based 3d object detection. In: Proceedings of the AAAI Conference on Artificial Intelligence, vol 1, pp 221–229
- Cheng Z, Liang J, Choi H, Tao G, Cao Z, Liu D, Zhang X (2022) Physical attack on monocular depth estimation with optimal adversarial patches. In: European Conference on Computer Vision, Springer, pp 514–532
- Choi J, Song Y, Kwak N (2021) Part-aware data augmentation for 3d object detection in point cloud. In: IEEE/RSJ International Conference on Intelligent Robots and Systems, pp 3391–3397
- Deng J, Shi S, Li P, Zhou W, Zhang Y, Li H (2021) Voxel r-cnn: Towards high performance voxel-based 3d object detection. In: Proceedings of the AAAI Conference on Artificial Intelligence, pp 1201–1209
- Dong X, Chen D, Zhou H, Hua G, Zhang W, Yu N (2020) Self-robust 3d point recognition via gather-vector guidance. In: 2020 IEEE/CVF Conference on Computer Vision and Pattern Recognition (CVPR), IEEE, pp 11513–11521
- Dong Y, Liao F, Pang T, Su H, Zhu J, Hu X, Li J (2018) Boosting adversarial attacks with momentum. In: Proceedings of the IEEE/CVF Conference on Computer Vision and Pattern Recognition, pp 9185–9193
- Dziugaite GK, Ghahramani Z, Roy DM (2016) A study of the effect of jpg compression on adversarial images. arXiv preprint arXiv:160800853
- Geiger A, Lenz P, Urtasun R (2012) Are we ready for autonomous driving? the kitti vision benchmark suite. In: Proceedings of the IEEE/CVF Conference on Computer Vision and Pattern Recognition, pp 3354–3361
- Goodfellow IJ, Shlens J, Szegedy C (2014) Explaining and harnessing adversarial examples. arXiv preprint arXiv:14126572
- Guo C, Rana M, Cisse M, van der Maaten L (2018) Countering adversarial images using input transformations. In: International Conference on Learning Representations
- Hamdi A, Rojas S, Thabet A, Ghanem B (2020) Advpc: Transferable adversarial perturbations on 3d point clouds. In: European Conference on Computer Vision, Springer, pp 241–257
- He C, Zeng H, Huang J, Hua XS, Zhang L (2020) Structure aware single-stage 3d object detection from point cloud. In: Proceedings of the IEEE/CVF Conference on Computer Vision and Pattern Recognition, pp 11870–11879
- Herrmann C, Sargent K, Jiang L, Zabih R, Chang H, Liu C, Krishnan D, Sun D (2022) Pyramid adversarial training improves vit performance. In: Proceedings of the IEEE/CVF Conference on Computer Vision and Pattern Recognition, pp 13419–13429
- Hu JS, Kuai T, Waslander SL (2022a) Point density-aware voxels for lidar 3d object detection. In: Proceedings of the IEEE/CVF Conference on Computer Vision and Pattern Recognition, pp 8469–8478
- Hu Z, Huang S, Zhu X, Sun F, Zhang B, Hu X (2022b) Adversarial texture for fooling person detectors in the physical world. In: Proceedings of the IEEE/CVF Conference on Computer Vision and Pattern Recognition, pp 13307–13316
- Jia J, Cao X, Gong NZ (2021) Intrinsic certified robustness of bagging against data poisoning attacks. In: Proceedings of the AAAI Conference on Artificial Intelligence, vol 35, pp 7961–7969
- Kerckhoffs A (1883) La cryptographie militaire. *Journal des sciences militaires* 9:5–38
- Kurakin A, Goodfellow IJ, Bengio S (2017) Adversarial machine learning at scale. In: International Conference on Learning Representations
- Kurakin A, Goodfellow IJ, Bengio S (2018) Adversarial examples in the physical world. In: Artificial intelligence safety and security, Chapman and Hall/CRC, pp 99–112
- Lang A, Vora S, Caesar H, Zhou L, Yang J, Beijbom O (2019a) Pointpillars: Fast encoders for object detection from point clouds. In: Proceedings of the IEEE/CVF Conference on Computer Vision and Pattern Recognition, pp 12689–12697
- Lang AH, Vora S, Caesar H, Zhou L, Yang J, Beijbom O (2019b) Pointpillars: Fast encoders for object detection from point clouds. In: Proceedings of the IEEE/CVF Conference on Computer Vision and Pattern Recognition, pp 12697–12705
- Lehner A, Gasperini S, Marcos-Ramiro A, Schmidt M, Mahani MAN, Navab N, Busam B, Tombari F (2022) 3d-vfield: Adversarial augmentation of point clouds for domain generalization in 3d object detection. In: Proceedings of the IEEE/CVF Conference on Computer Vision and Pattern Recognition, pp 17295–17304
- Li B, Chen C, Wang W, Carin L (2019) Certified adversarial robustness with additive noise. *Advances in neural information processing systems* 32
- Liu D, Hu W (2022) Imperceptible transfer attack and defense on 3d point cloud classification. *IEEE Transactions on Pattern Analysis and Machine Intelligence*
- Liu D, Yu R, Su H (2019) Extending adversarial attacks and defenses to deep 3d point cloud classifiers. In: 2019 IEEE International Conference on Image Processing (ICIP), IEEE, pp 2279–2283

- Liu D, Yu R, Su H (2020) Adversarial shape perturbations on 3d point clouds. In: European Conference on Computer Vision, Springer, pp 88–104
- Liu H, Jia J, Gong NZ (2021) Pointguard: Provably robust 3d point cloud classification. In: Proceedings of the IEEE/CVF Conference on Computer Vision and Pattern Recognition (CVPR), pp 6186–6195
- Madry A, Makelov A, Schmidt L, Tsipras D, Vladu A (2018) Towards deep learning models resistant to adversarial attacks. In: International Conference on Learning Representations, pp 1–28
- Osadchy M, Hernandez-Castro J, Gibson S, Dunkelman O, Pérez-Cabo D (2017) No bot expects the deepcaptcha! introducing immutable adversarial examples, with applications to captcha generation. *IEEE Transactions on Information Forensics and Security* 12(11):2640–2653
- Paszke A, Gross S, Massa F, Lerer A, Bradbury J, Chanan G, Killeen T, Lin Z, Gimelshein N, Antiga L, Desmaison A, Köpf A, Yang EZ, DeVito Z, Raison M, Tejani A, Chilamkurthy S, Steiner B, Fang L, Bai J, Chintala S (2019) Pytorch: An imperative style, high-performance deep learning library. In: Wallach HM, Larochelle H, Beygelzimer A, d'Alché-Buc F, Fox EB, Garnett R (eds) *Advances in Neural Information Processing Systems*, pp 8024–8035
- Qi C, Su H, Mo K, Guibas LJ (2017) Pointnet: Deep learning on point sets for 3d classification and segmentation. In: Proceedings of the IEEE conference on computer vision and pattern recognition, pp 652–660
- Shi S, Wang X, Li H (2019) Pointcnn: 3d object proposal generation and detection from point cloud. In: Proceedings of the IEEE/CVF conference on computer vision and pattern recognition, pp 770–779
- Shi S, Guo C, Jiang L, Wang Z, Shi J, Wang X, Li H (2020a) Pv-rnn: Point-voxel feature set abstraction for 3d object detection. In: Proceedings of the IEEE/CVF Conference on Computer Vision and Pattern Recognition, pp 10529–10538
- Shi S, Wang Z, Shi J, Wang X, Li H (2020b) From points to parts: 3d object detection from point cloud with part-aware and part-aggregation network. *IEEE Transactions on Pattern Analysis and Machine Intelligence* 43(8):2647–2664
- Sun J, Cao Y, Chen QA, Mao ZM (2020a) Towards robust {LiDAR-based} perception in autonomous driving: General black-box adversarial sensor attack and countermeasures. In: 29th USENIX Security Symposium (USENIX Security 20), pp 877–894
- Sun J, Cao Y, Choy CB, Yu Z, Anandkumar A, Mao ZM, Xiao C (2021) Adversarially robust 3d point cloud recognition using self-supervisions. *Advances in Neural Information Processing Systems* 34:15498–15512
- Sun P, Kretschmar H, Dotiwala X, Chouard A, Patnaik V, Tsui P, Guo J, Zhou Y, Chai Y, Caine B, Vasudevan V, Han W, Ngiam J, Zhao H, Timofeev A, Ettinger S, Krivokon M, Gao A, Joshi A, Zhang Y, Shlens J, Chen Z, Anguelov D (2020b) Scalability in perception for autonomous driving: Waymo open dataset. In: Proceedings of the IEEE/CVF Conference on Computer Vision and Pattern Recognition, pp 2443–2451
- Szegedy C, Zaremba W, Sutskever I, Bruna J, Erhan D, Goodfellow I, Fergus R (2013) Intriguing properties of neural networks. *International Conference on Learning Representations* pp 1–10
- Tramèr F, Kurakin A, Papernot N, Goodfellow I, Boneh D, McDaniel P (2018) Ensemble adversarial training: Attacks and defenses. In: *International Conference on Learning Representations*
- Tsai T, Yang K, Ho TY, Jin Y (2020) Robust adversarial objects against deep learning models. In: Proceedings of the AAAI Conference on Artificial Intelligence, vol 34, pp 954–962
- Tu J, Ren M, Manivasagam S, Liang M, Yang B, Du R, Cheng F, Urtasun R (2020) Physically realizable adversarial examples for lidar object detection. In: Proceedings of the IEEE/CVF conference on computer vision and pattern recognition, Computer Vision Foundation / IEEE, pp 13713–13722
- Tu J, Li H, Yan X, Ren M, Chen Y, Liang M, Bitar E, Yumer E, Urtasun R (2021) Exploring adversarial robustness of multi-sensor perception systems in self driving. In: 5th Annual Conference on Robot Learning, pp 1–12
- Wen Y, Lin J, Chen K, Chen CP, Jia K (2020) Geometry-aware generation of adversarial point clouds. *IEEE Transactions on Pattern Analysis and Machine Intelligence*
- Wicker M, Kwiatkowska M (2019) Robustness of 3d deep learning in an adversarial setting. In: Proceedings of the IEEE/CVF Conference on Computer Vision and Pattern Recognition, pp 11767–11775
- Xiang C, Qi CR, Li B (2019) Generating 3d adversarial point clouds. In: Proceedings of the IEEE/CVF Conference on Computer Vision and Pattern Recognition, pp 9136–9144
- Xu W, Evans D, Qi Y (2017) Feature squeezing: Detecting adversarial examples in deep neural networks. arXiv preprint arXiv:1704.01155
- Yan Y, Mao Y, Li B (2018) Second: Sparsely embedded convolutional detection. *Sensors* 18(10):3337
- Yang Z, Sun Y, Liu S, Jia J (2020) 3dssd: Point-based 3d single stage object detector. In: Proceedings of the IEEE/CVF Conference on Computer Vision and Pattern Recognition, pp 11040–11048
- Zhang Y, Hu Q, Xu G, Ma Y, Wan J, Guo Y (2022) Not all points are equal: Learning highly efficient point-based detectors for 3d lidar point clouds. In: Proceedings of the IEEE/CVF Conference on Computer Vision and Pattern Recognition, pp 18953–18962

- Zheng T, Chen C, Yuan J, Li B, Ren K (2019) Pointcloud saliency maps. In: Proceedings of the IEEE/CVF International Conference on Computer Vision, pp 1598–1606
- Zhou H, Chen K, Zhang W, Fang H, Zhou W, Yu N (2019) Dup-net: Denoiser and upsampler network for 3d adversarial point clouds defense. In: Proceedings of the IEEE/CVF International Conference on Computer Vision, pp 1961–1970
- Zhou Y, Tuzel O (2018) Voxelnet: End-to-end learning for point cloud based 3d object detection. In: Proceedings of the IEEE/CVF Conference on Computer Vision and Pattern Recognition, pp 4490–4499

Appendix

A. Result of Absolute mAP Under Attacks

In addition to the mAP ratio of detectors under adversarial attacks, we also report the absolute mAP values from Table 14 to Table 23. As shown in Table 16, the PDV achieves the best detection accuracy on the clean input but sub-optimal performance under PGD-based point perturbation attack. The result implies that we should also take the robustness of 3D detectors into consideration in addition to detection accuracy.

Table 14: The absolute mAP of various 3D detectors on the KITTI dataset under FGM-based point perturbation attack with different ϵ values. $\epsilon=0$ denotes the mAP on clean input.

Detector	ϵ (cm)						
	0	0.5	1	3	5	7	10
Second	69.64	69.00	68.29	67.39	65.56	63.61	57.82
Voxel-RCNN	74.36	73.88	73.68	74.17	72.45	71.13	67.21
PDV	75.91	74.97	73.71	70.14	67.15	57.99	45.05
PointPillar	67.22	59.96	56.56	45.98	42.66	41.08	41.06
Part-A ²	74.85	72.80	74.33	73.07	72.98	71.18	67.10
PV-RCNN	71.03	71.03	70.27	67.67	65.99	61.50	51.24
3DSSD	71.48	67.41	66.08	58.11	56.38	49.70	42.21
PointRCNN	72.62	67.44	63.95	56.62	50.89	44.27	32.97

Table 15: The absolute mAP of various 3D detectors on the KITTI dataset under MI-FGM based point perturbation attack with different ϵ values.

Detector	ϵ (cm)						
	0	0.5	1	3	5	7	10
Second	69.64	68.91	68.24	67.37	65.63	63.94	57.38
Voxel-RCNN	74.36	74.03	74.22	73.65	72.54	70.48	68.56
PDV	75.91	73.80	71.88	66.78	58.35	49.01	37.14
PointPillar	67.22	60.30	54.88	39.38	32.07	28.59	26.58
Part-A ²	74.85	73.03	73.21	73.15	73.78	70.56	67.96
PV-RCNN	71.03	70.58	70.21	66.09	60.78	50.72	32.68
3DSSD	71.48	66.26	63.25	49.98	39.71	26.71	15.92
PointRCNN	72.62	65.13	62.60	48.43	34.14	25.29	12.90

Table 16: The absolute mAP of various 3D detectors on the KITTI dataset under PGD-based point perturbation attack with different ϵ values.

Detector	ϵ (cm)						
	0	0.5	1	3	5	7	10
Second	69.64	69.34	68.01	66.24	64.03	59.71	49.30
Voxel-RCNN	74.36	73.14	74.01	72.29	70.81	68.13	59.67
PDV	75.91	75.03	74.13	72.10	67.10	62.02	46.77
PointPillar	67.22	61.03	54.78	35.75	22.09	12.66	4.90
Part-A ²	74.85	73.28	73.29	73.01	71.80	68.28	56.22
PV-RCNN	71.03	70.89	68.36	66.43	63.04	54.39	35.37
3DSSD	71.48	68.78	63.47	54.96	40.56	26.77	13.63
PointRCNN	72.62	67.03	65.46	52.52	39.88	25.68	10.49

Table 17: The absolute mAP of various 3D detectors on the KITTI dataset under point detachment attack with different ratios of dropped points.

Detector	Ratio of dropped points (%)						
	0	0.05	0.1	0.3	0.5	1	2
Second	69.64	68.60	64.83	62.92	58.31	54.31	47.30
Voxel-RCNN	74.36	74.02	71.06	65.64	62.62	58.18	48.21
PDV	75.91	73.36	68.46	62.10	54.57	49.11	36.54
PointPillar	67.22	65.70	63.39	58.79	55.67	51.92	43.79
Part-A ²	74.85	74.85	72.15	67.29	63.67	58.98	48.31
PV-RCNN	71.03	70.44	68.87	64.59	62.40	56.48	44.90
3DSSD	71.48	69.84	66.16	60.33	59.21	50.81	41.28
PointRCNN	72.62	71.61	66.66	63.07	61.57	57.47	49.74

Table 18: The absolute mAP of various 3D detectors on the KITTI dataset under point attachment attack with different ϵ values. The number of added points is set to 164.

Detector	ϵ (m)						
	0	0.05	0.1	0.3	0.5	0.7	1
Second	69.64	66.03	64.72	59.54	53.59	58.15	60.40
Voxel-RCNN	74.36	74.24	73.07	68.01	62.28	63.82	66.82
PDV	75.91	72.23	67.11	48.69	48.29	49.98	58.49
PointPillar	67.22	65.45	64.21	60.37	57.80	55.40	55.39
Part-A ²	74.85	73.13	73.56	69.30	68.47	70.53	71.47
PV-RCNN	71.03	70.98	68.70	64.32	63.05	62.53	62.52
3DSSD	71.48	49.28	45.29	48.80	52.81	53.91	59.23
PointRCNN	72.62	69.42	63.55	52.91	52.85	53.87	56.80

Table 19: The absolute mAP of various 3D detectors on the Waymo dataset under FGM-based point perturbation attack with different ϵ values.

Detector	ϵ (cm)						
	0	0.5	1	3	5	7	10
Second	59.342	58.80	58.20	57.43	55.87	54.21	49.27
Voxel-RCNN	63.245	62.83	62.66	63.08	61.62	60.49	57.16
PDV	68.640	67.79	66.65	63.42	60.72	52.43	40.74
PointPillar	57.016	50.86	47.97	39.00	36.18	34.84	34.83
Part-A ²	65.719	63.92	65.26	64.15	64.08	62.50	58.91
PV-RCNN	65.603	65.60	64.90	62.50	60.95	56.80	47.32
3DSSD	60.127	56.70	55.59	48.88	47.43	41.81	35.50
PointRCNN	61.870	57.46	54.49	48.24	43.36	37.72	28.09

Table 20: The absolute mAP of various 3D detectors on the Waymo dataset under MI-FGM based point perturbation attack with different ϵ values.

Detector	ϵ (cm)						
	0	0.5	1	3	5	7	10
Second	59.342	59.08	57.92	55.87	53.46	52.41	48.75
Voxel-RCNN	63.245	62.95	62.94	62.19	60.99	58.17	54.52
PDV	68.640	67.30	64.38	58.57	51.27	42.46	29.00
PointPillar	57.016	52.57	48.14	35.02	25.24	19.11	13.11
Part-A ²	65.719	65.65	65.59	65.08	63.85	62.67	59.16
PV-RCNN	65.603	64.51	64.00	60.58	58.20	53.47	46.08
3DSSD	60.127	57.02	53.51	43.55	31.91	20.82	13.74
PointRCNN	61.870	56.89	54.20	41.84	28.29	19.27	9.45

Table 21: The absolute mAP of various 3D detectors on the Waymo dataset under PGD-based point perturbation attack with different ϵ values.

Detector	ϵ (cm)						
	0	0.5	1	3	5	7	10
Second	59.342	59.16	58.11	55.88	52.40	49.48	42.92
Voxel-RCNN	63.245	63.06	62.80	62.23	62.08	59.86	56.74
PDV	68.640	68.00	66.32	63.65	59.41	54.53	37.30
PointPillar	57.016	53.42	49.53	34.53	18.34	8.95	2.82
Part-A ²	65.719	65.77	65.70	64.61	63.30	62.83	58.66
PV-RCNN	65.603	64.40	63.87	61.58	59.05	54.93	47.50
3DSSD	60.127	58.58	54.03	47.96	32.07	20.83	9.81
PointRCNN	61.870	57.73	56.57	46.38	33.03	19.27	7.50

Table 22: The absolute mAP of various 3D detectors on the Waymo dataset under point detachment attack with different ratios of dropped points.

Detector	Ratio of dropped points (%)						
	0	0.05	0.1	0.3	0.5	1	2
Second	59.342	58.26	55.99	53.62	51.95	50.31	45.06
Voxel-RCNN	63.245	60.62	57.64	54.22	51.78	48.40	41.02
PDV	68.640	64.92	60.39	54.92	49.65	46.70	37.28
PointPillar	57.016	56.55	54.79	53.13	52.20	50.86	46.84
Part-A ²	65.719	63.23	59.64	56.72	53.99	51.73	45.26
PV-RCNN	65.603	61.97	56.61	50.31	46.16	41.26	29.43
3DSSD	60.127	56.52	52.99	49.22	48.40	41.71	33.54
PointRCNN	61.870	58.30	53.78	52.19	50.35	48.00	39.73

Table 23: The absolute mAP of various 3D detectors on the Waymo dataset under point attachment attack with different ϵ values. $\epsilon=0$ denotes the mAP on clean input. The number of added points is set to 500.

Detector	ϵ (m)						
	0	0.05	0.1	0.3	0.5	0.7	1
Second	59.342	58.26	56.53	50.53	46.25	44.56	45.61
Voxel-RCNN	63.245	54.66	54.09	57.21	58.95	61.16	62.23
PDV	68.640	67.29	61.19	43.57	42.69	44.01	47.33
PointPillar	57.016	55.93	55.45	51.53	48.89	46.81	46.27
Part-A ²	65.719	65.65	64.58	59.75	54.76	53.75	54.60
PV-RCNN	65.603	60.01	59.32	60.06	60.26	61.85	62.56
3DSSD	60.127	40.58	37.32	41.64	46.28	49.11	54.24
PointRCNN	61.870	54.41	50.73	45.75	45.94	48.26	51.20